Nanoscale

PAPER

View Article Online
View Journal | View Issue

Cite this: *Nanoscale*, 2016, **8**, 16017

One-step fabrication of large-area ultrathin MoS_2 nanofilms with high catalytic activity for photovoltaic devices†

Jia Liang,[a] Jia Li,[b] Hongfei Zhu,[a] Yuxiang Han,[b] Yanrong Wang,[a] Caixing Wang,[a] Zhong Jin,*[a] Gengmin Zhang*[b] and Jie Liu*[a,c]

Received 5th May 2016,
Accepted 7th August 2016

DOI: 10.1039/c6nr03635j

www.rsc.org/nanoscale

Here we report a facile one-step solution-phase process to directly grow ultrathin MoS_2 nanofilms on a transparent conductive glass as a novel high-performance counter electrode for dye-sensitized solar cells. After an appropriate reaction time, the entire surface of the conductive glass substrate was uniformly covered by ultrathin MoS_2 nanofilms with a thickness of only several stacked layers. Electrochemical impedance spectroscopy and cyclic voltammetry reveal that the MoS_2 nanofilms possess excellent catalytic activity towards tri-iodide reduction. When used in dye-sensitized solar cells, the MoS_2 nanofilms show an impressive energy conversion efficiency of 8.3%, which is higher than that of a Pt-based electrode and very promising to be a desirable alternative counter electrode. Considering their ultrathin thickness, superior catalytic activity, simple preparation process and low cost, the as-prepared MoS_2 nanofilms with high photovoltaic performance are expected to be widely employed in dye-sensitized solar cells.

Aroused by the research on graphene in recent years, two-dimensional (2D) layered transition metal dichalcogenides (LTMDs) have attracted intensive attention because of their unique physical and chemical properties.[1–5] Molybdenum disulfide (MoS_2), as a typical 2D LTMD material, has attracted a great deal of attention recently due to its desirable electronic structure.[6–10] Specifically, the sandwiched S–Mo–S layers in a hexagonally packed MoS_2 lattice are held together by weak van der Waals bonds.[11,12] In addition, compared with bulk MoS_2, more active sites can be found on the edges of MoS_2 nanosheets. Owing to its unique structure and properties, MoS_2 has been employed in diverse fields such as transistors,[13–15] photodetectors,[16,17] Li-ion batteries,[18–21] hydrogen evolution reactions,[22–29] and dye-sensitized solar cells (DSSCs).[30–37]

In the last few years, several different approaches (*e.g.*, chemical vapor deposition (CVD) method and hydrothermal method) have been developed to prepare MoS_2 nanofilms on various substrates.[32–37] However, so far, most of the reported MoS_2-based substrates still cannot meet the demands of large-scale production because of their complicated and time-consuming preparation processes.[30–37] Moreover, to directly grow 2D materials on glass substrates for overcoming the disadvantages caused by transfer is a challenging task and has attracted intensive attention. For instance, Liu *et al.* reported the CVD growth of high-quality graphene disks on a glass substrate.[38,39] However, for MoS_2, few studies have been done in this field. Therefore, it is desirable to look for greatly simplified approaches for directly preparing layered MoS_2 atomic layers with extraordinary properties on the desired substrate.

In this study, we report a one-step and low-cost solution-phase method to directly fabricate large-area ultrathin MoS_2 nanofilms on a fluorine-doped tin oxide (FTO) glass substrate. The conductive glass substrate with MoS_2 nanofilms obtained from the reaction of Na_2MoO_4 and C_2H_5NS was named MoS_2-x, where x corresponds to the reaction time (x = 5, 10 or 15 h). It was found that all of the surface of the conductive glass substrate would be covered by the ultrathin MoS_2 nanofilms after an appropriate reaction time (15 h). According to the electrochemical analyses, including electrochemical impedance spectroscopy (EIS) and cyclic voltammetry (CV), the MoS_2 nanofilms exhibited superior catalytic activity towards tri-iodide reduction. Furthermore, we employed large-area ultrathin MoS_2 nanofilms on the conductive glass substrate as a counter electrode in the DSSCs. The MoS_2-based electrode displayed an impressive photovoltaic performance as high as

[a]*Key Laboratory of Mesoscopic Chemistry of MOE and Collaborative Innovation Center of Chemistry for Life Sciences, School of Chemistry and Chemical Engineering, Nanjing University, Nanjing 210093, China. E-mail: zhongjin@nju.edu.cn*
[b]*Key Laboratory for the Physics and Chemistry of Nanodevices, Department of Electronics, Peking University, Beijing 100871, China. E-mail: zgmin@pku.edu.cn*
[c]*Department of Chemistry, Duke University, Durham, North Carolina 27708, USA. E-mail: j.liu@duke.edu*

†Electronic supplementary information (ESI) available. See DOI: 10.1039/c6nr03635j

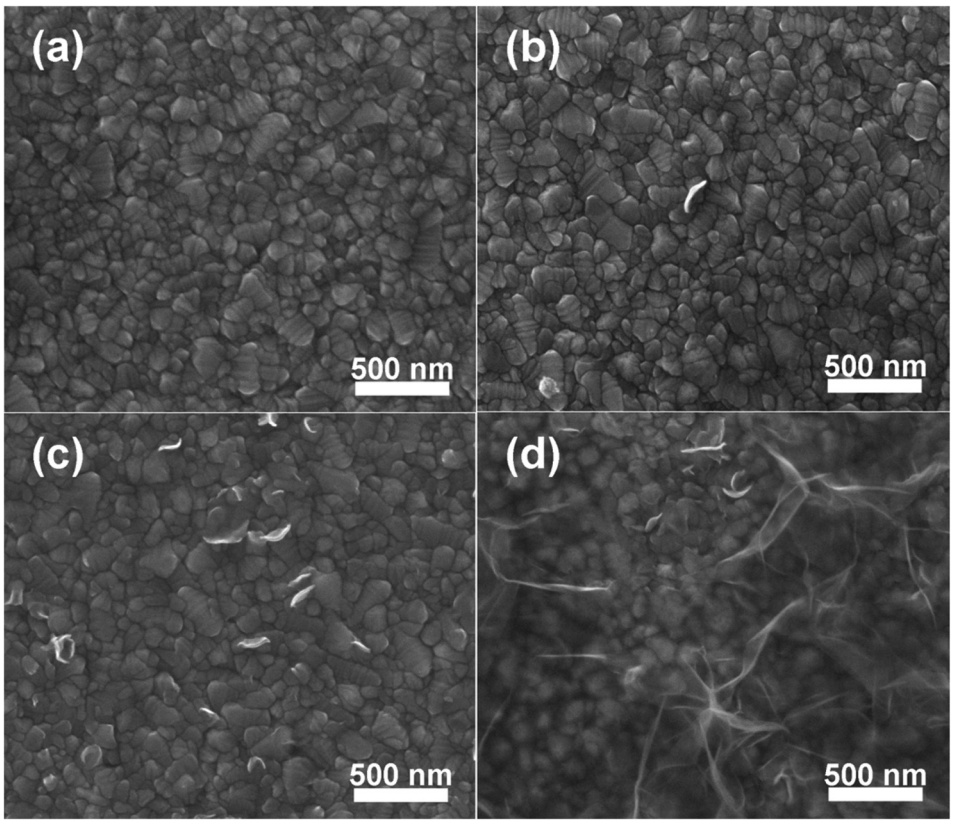

Fig. 1 SEM images of (a) the pristine FTO glass and the as-prepared ultrathin MoS_2 nanofilms of (b) MoS_2-5, (c) MoS_2-10, and (d) MoS_2-15 samples grown on FTO glass substrates, respectively.

8.3%, which was better than that of the DSSCs based on platinized counter electrodes.

Fig. 1a shows a typical scanning electron microscopy (SEM) image of a commercial FTO glass substrate; the clean surface is covered by tin dioxide (SnO_2) nanocrystals. Different from the pristine FTO glass, MoS_2 nanofilms were found covering the substrates of the MoS_2-5 and MoS_2-10 samples after reaction times of 5 h and 10 h, respectively (Fig. 1b and c). Meanwhile, the coverage of MoS_2 nanofilms highly increased as the reaction time increased from 5 h to 10 h. Fig. 1d shows the SEM image of a MoS_2-15 sample; the whole surface of the FTO glass is uniformly covered by ultrathin MoS_2 nanofilms, which is beneficial for its application as a counter electrode in DSSCs. In principle, the area of the FTO substrate covered with as-grown MoS_2 nanofilms is only limited by the diameter of the autoclave, which can be easily scaled up by increasing the size of the autoclave. Fig. S1† shows optical images of the pristine FTO substrate and the MoS_2-15 sample with a large area of 4 cm × 4 cm.

To further characterize the structural features of ultrathin MoS_2 nanofilms, transmission electron microcopy (TEM) and high-resolution TEM (HRTEM) studies were performed on the MoS_2-15 nanofilms. Fig. 2a shows a typical TEM image of the MoS_2-15 nanofilm loaded on a TEM grid, which reveals that most areas of the MoS_2 nanofilm are very uniform and with a flat and smooth surface. Fig. 2b displays a HRTEM image of the MoS_2-15 nanofilm; the cross-section of the MoS_2 nanofilm can be clearly observed and indicates a thickness of only a few atomic layers. The distance between two adjacent atomic planes is 0.62–0.63 nm, which is in accordance with the interplanar distance of the (002) planes of crystalline hexagonal MoS_2.

To identify the compositions of MoS_2-x nanofilms (x = 5, 10, 15), the characterization of X-ray photoelectron spectroscopy (XPS) was carried out, as shown in Fig. 3a. The C 1s peak, which can be found in all three samples and is generally believed to have arisen from the adventitious carbon caused by exposure to the atmosphere, is used as the standard for binding energy calibration. With the energy of the C 1s peak set at 284.6 eV, the energy of each peak in the three samples was determined. Besides the C 1s peak, the spectra are dominated by the photoelectron peaks of Sn, O, Mo, and S. Among them, the peaks of Sn and O are derived from the SnO_2 film on the FTO glass substrates. The binding energies of Mo $3d_{3/2}$, Mo $3d_{5/2}$, S $2p_{1/2}$, and S $2p_{3/2}$ are located at 231.5 ± 0.2, 228.2 ± 0.3, 162.2 ± 0.2, and 161.1 ± 0.3 eV, respectively, which are in agreement with previous studies and confirm that the chemical composition of the as-obtained nanofilm is MoS_2.[26,27] Much weaker peaks of Mo and S can be found in the XPS spectrum of MoS_2-5 compared to MoS_2-10 and MoS_2-

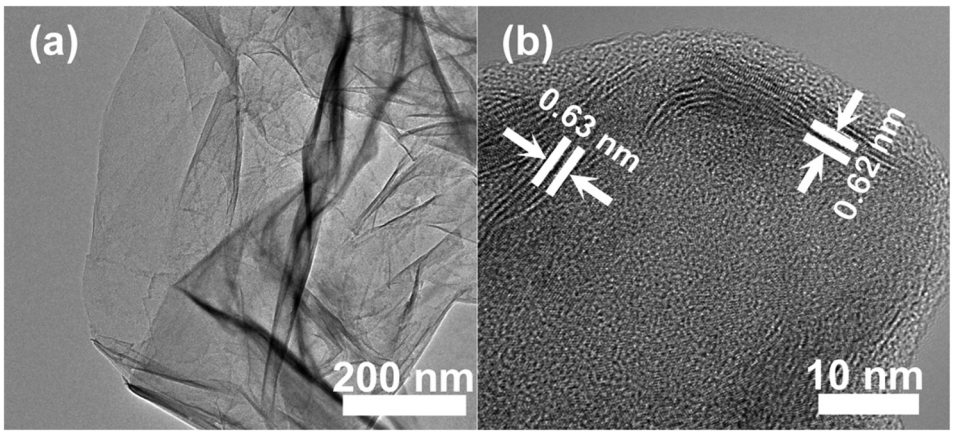

Fig. 2 (a) TEM and (b) HRTEM images of the MoS_2-15 nanofilms.

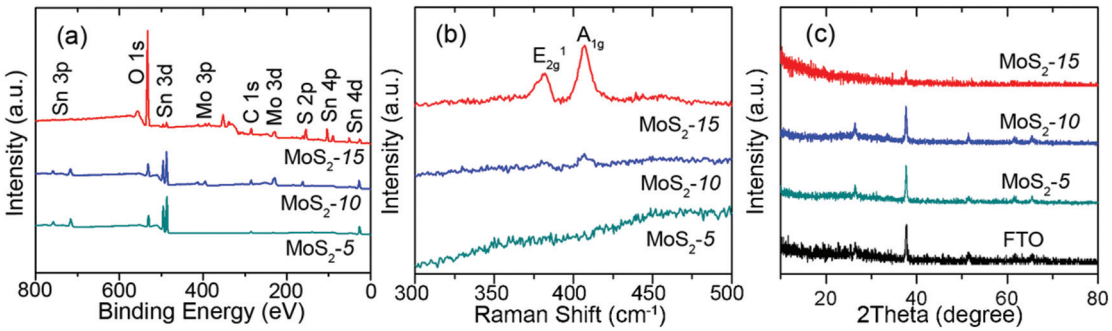

Fig. 3 (a) XPS, (b) Raman and (c) XRD spectra of MoS_2-x (x = 5, 10 or 15) nanofilms grown on FTO glass substrates, respectively.

15, indicating that the amount of MoS_2 is lower, which is ascribed to the shorter reaction time and lower surface coverage. On increasing the reaction time, higher Mo and S peaks can be found in the corresponding MoS_2-15 sample, because more areas on the surface of the FTO glass substrate are covered by the MoS_2 nanofilm, which is also in accordance with the SEM image (Fig. 1d).

The results acquired from Raman spectroscopy (Fig. 3b) also confirmed the growth of MoS_2 nanofilms. From MoS_2-5 to MoS_2-15, the Raman peaks emerging at 378 and 405 cm^{-1} correspond to the $E_{2g}{}^1$ and A_{1g} modes of MoS_2 respectively. The intensity of $E_{2g}{}^1$ and A_{1g} modes rise from minimal to high as the reaction time increases, indicating that more MoS_2 nanofilms are grown on FTO glass substrates. The two Raman peaks also provide insights into the structure of the MoS_2 nanofilm. The $E_{2g}{}^1$ mode, also called the in-plane Mo–S phonon mode, was excited from the terrace-terminated film, while the A_{1g} mode, also called the out of plane Mo–S phonon mode, was excited for the edge-terminated film.[40] The relative integral peak intensity of these two phonon modes can give some texture information of the layered MoS_2 nanofilms. As shown in the Raman spectrum of MoS_2-15 (Fig. 3b), the integral intensity of the A_{1g} mode is twice that of the $E_{2g}{}^1$ mode, indicating that the vibration of the A_{1g} mode is predominant in the layered MoS_2 nanofilms. Fig. 3c shows the XRD patterns of pristine FTO glass and MoS_2-x nanofilms, respectively. The characteristic peaks of MoS_2 are very weak, owing to the ultrathin thickness. The intensity of FTO peaks decreases as the growth time increases, indicating that more and more area of the FTO substrate is covered by MoS_2; thus some XRD signals of FTO are concealed.

The platinized-FTO glass and MoS_2-x covered FTO glass counter electrodes were respectively assembled into DSSCs (Fig. 4a), and their current density–voltage (J–V) characteristics were measured. The photovoltaic performance was characterized by four important parameters, including short-circuit density (J_{SC}), open-circuit voltage (V_{OC}), fill factor (FF), and conversion efficiency (η). Fig. 4b shows the J–V plots of the DSSCs using the pristine FTO, platinized-FTO and MoS_2-x covered FTO glass substrates as the counter electrodes under illumination, respectively. The corresponding measured photovoltaic parameters are listed in Table 1. The DSSC with a pristine-FTO glass counter electrode displays a very poor photovoltaic performance, because the pristine FTO electrode has little catalytic activity for tri-iodide reduction. In contrast, the DSSCs based on platinized-FTO and MoS_2-x covered FTO glass electrodes exhibit much better photovoltaic performances. The Pt-based DSSC has a J_{SC} of 13.77 mA cm^{-2}, a V_{OC} of

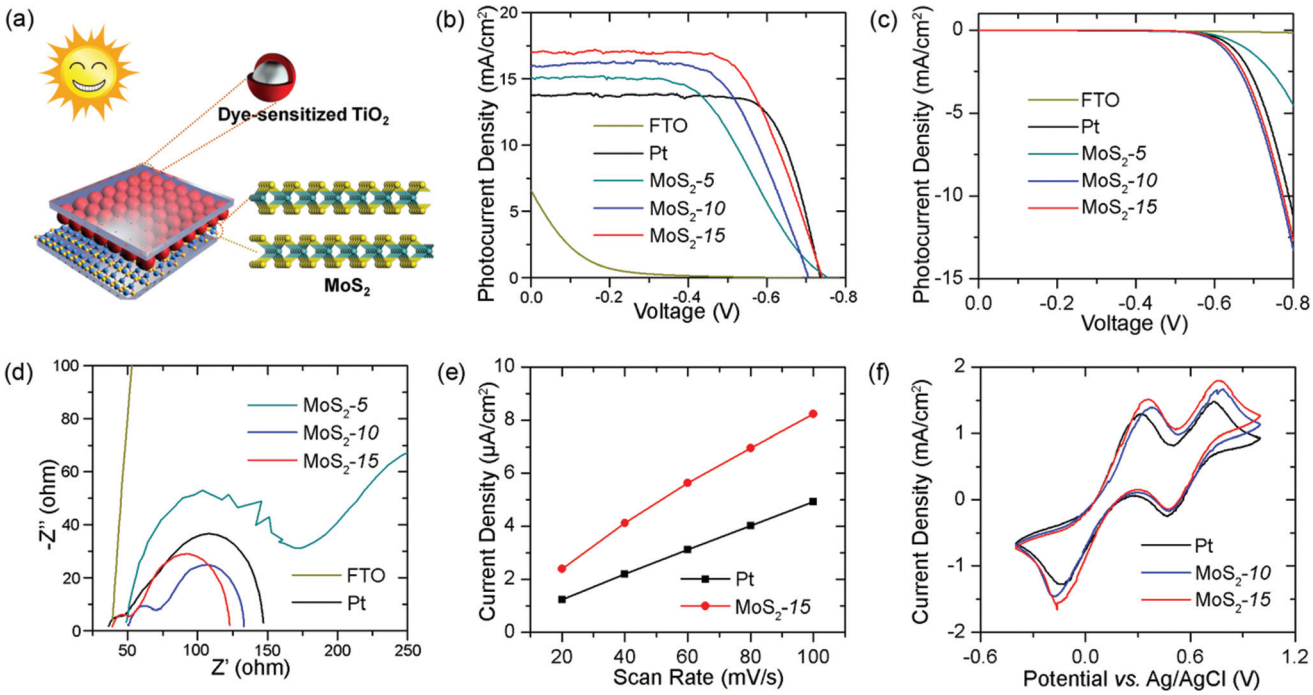

Fig. 4 (a) Schematic diagram of a DSSC with a counter electrode based on MoS_2 nanofilms. *J–V* plots of DSSCs using pristine, platinized, MoS_2-5 based, MoS_2-10 based, and MoS_2-15 based FTO glass substrates as counter electrodes under (b) full light conditions and (c) dark conditions, respectively. (d) Nyquist plots of DSSCs using pristine, platinized, MoS_2-5 based, MoS_2-10 based, and MoS_2-15 based FTO glass substrates as the counter electrodes under dark conditions. (e) Linear fitting of the capacitive current densities of Pt-based and MoS_2-15-based counter electrode, respectively. (f) CV curves of Pt-based, MoS_2-10 based, and MoS_2-15 based counter electrodes for iodide species at a scanning rate of 100 mV s^{-1}.

Table 1 Photovoltaic parameters and EIS parameters of the DSSCs using pristine, platinized, MoS_2-5 based, MoS_2-10 based, and MoS_2-15 based FTO glass substrates as the counter electrodes

Electrodes	J_{SC} (mA cm^{-2})	V_{OC} (V)	FF	η (%)	R_s/Ω	R_{ct}/Ω	$C_\mu/\mu F$
FTO	6.59	−0.68	0.05	0.24	—	—	—
Pt	13.77	−0.74	0.74	7.53	36.3	13.1	3.9
MoS_2-5	15.15	−0.76	0.52	5.96	50.9	118.8	1.8
MoS_2-10	15.94	−0.71	0.63	7.14	50.4	21.2	2.8
MoS_2-15	16.96	−0.74	0.66	8.28	38.8	12.9	5.3

0.74 V, an FF of 0.74, and a η of 7.53%. For the three MoS_2-*x* based DSSCs, they show gradually improved photovoltaic performances as the growth time *x* increases, which is ascribed to the increased coverage of MoS_2 nanofilms grown on the surface of the FTO glass. Compared with the Pt-based DSSC, all three MoS_2-*x* based DSSCs exhibit comparable V_{OC}, smaller FF, but much larger J_{SC}, which results in an excellent η of 6.0%–8.3%. These values are equivalent to or even higher than that of the Pt-based DSSC. The highest η among these different DSSCs is obtained from the DSSC based on the MoS_2 nanofilms with the longest growth time (MoS_2-15). Fig. 4c shows the *J–V* plots of DSSCs using pristine FTO, platinized-FTO and MoS_2-*x* covered FTO glass substrates as counter electrodes under dark conditions, respectively. The pristine FTO based DSSC exhibits the smallest dark current density among all the DSSCs, while MoS_2-10 based and MoS_2-15 based DSSCs show slightly higher dark current densities than Pt-based DSSC, in accordance with the results under illumination. The *J–V* curves measured under illumination and dark conditions indicate that the MoS_2 based counter electrode is a very promising candidate to replace the traditional Pt-based counter electrode in DSSCs.

Fig. 4b and Table 1 show that the FF, as an important parameter of the DSSCs, undergoes a dramatic change with the growth time of the three MoS_2-*x* based counter electrodes. It should be noted that the FF is determined by the series resistance of the whole solar cell, such as the sheet resistances of working and counter electrodes, the electron transport resistance and the ion transport resistance.[41] It is known that MoS_2, as a transition metal sulfide with an atomic layered structure, is a semiconductor with a bandgap of 1.2–2.1 eV.[42,43] Therefore, when MoS_2 nanofilms are used as the catalyst in the counter electrode, their intrinsic characteristics will result in a larger sheet resistance than that of the Pt-based counter

electrode. This result is also revealed by the EIS analysis, as shown in Fig. 4d. Thus, in the MoS_2-based DSSCs, the increased series resistance results in low FF, especially in MoS_2-5 based and MoS_2-10 based DSSCs. J_{SC} is another important factor for the photovoltaic performance of a DSSC. In Fig. 4b and Table 1, the J_{SC} values of the three MoS_2-based DSSCs are larger than that of the Pt-based DSSC. The corresponding DSSC of the MoS_2-15 based counter electrode displays the highest J_{SC}. This may have resulted from the large surface area of the MoS_2 nanofilm owing to its 2D layered structure, which makes the oxidized species in the electrolyte rapidly and effectively capture electrons at the counter electrode/electrolyte interface, leading to a significant decrease of charge recombination and the corresponding increase of J_{SC}. Accordingly, because the increase in J_{SC} is much more remarkable than the decrease in FF, the efficiency of DSSC is considerably enhanced by using the MoS_2-15 covered FTO glass as the counter electrode.

To obtain better insight into the kinetics of the interfacial charge transfer process within the DSSCs, the EIS was measured. Fig. 4d shows the Nyquist plots of the DSSCs using the above-mentioned five kinds of different counter electrodes under dark conditions. Without any catalyst (Pt or MoS_2) coated on the FTO glass, the pristine FTO glass based DSSC displays the worst charge transfer performance among these DSSCs. Typically, the onset point of the first semicircle in the high frequency region corresponds to the Ohmic series resistance of the substrate (R_s). The semicircle in the low-frequency region corresponds to the charge transfer at the interface of the TiO_2/dye/electrolyte, and the semicircle in the high-frequency region is attributed to the charge transfer at the interface of the counter electrode/electrolyte, including the charge transfer resistance (R_{ct}) and the corresponding capacitance (C_μ) at the interface of the counter electrode/electrolyte. To estimate the resistance parameters at the interface of the counter electrode/electrolyte of the Pt-based and all three MoS_2-based DSSCs, the raw data were fitted using the Z-view software with the equivalent circuit (Fig. S2†) and the corresponding parameters are listed in Table 1. As mentioned above, due to the semiconductive characteristics of MoS_2, the R_s values of the three MoS_2-based DSSCs are larger than that of the Pt-based DSSC. However, the MoS_2-15 based DSSC shows a comparable R_s value relative to the Pt-based DSSC, owing to the large-area and continuous MoS_2 nanofilms uniformly covered on the substrate. The R_{ct} value of the MoS_2-5 based DSSC is 118.8 Ω, which is much larger than that of the MoS_2-10 based DSSC (21.2 Ω). This is mainly due to the higher MoS_2 coverage of the MoS_2-10 based counter electrode than that of the MoS_2-5 based counter electrode, as confirmed by SEM (Fig. 1), XPS (Fig. 3a), and Raman results (Fig. 3b). The MoS_2-15 based DSSC has a slightly lower R_{ct} value (12.9 Ω) than the Pt-based DSSC (13.1 Ω), indicating that the MoS_2-15 based counter electrode has superior electrocatalytic activity compared to all other counter electrodes, including the Pt-based counter electrode. C_μ is expected to be proportional to the specific surface area. Therefore, a larger C_μ value refers to a larger catalytically-active surface area and thereby refers to a better electrocatalytic activity at the interface of the electrode/electrolyte. Table 1 shows that the C_μ of MoS_2-x based DSSCs increases as x increases, and finally reaches the largest value in MoS_2-15 based DSSC. This is because most of the area of the FTO substrate on the MoS_2-15 based electrode is covered by MoS_2 nanofilms when compared to MoS_2-5 and MoS_2-10 (Fig. 1). Furthermore, the C_μ value of MoS_2-15 based DSSC is higher than that of Pt-based DSSC, suggesting that the MoS_2-15 based counter electrode possesses a larger catalytically-active surface area than the Pt-based counter electrode, and thus the MoS_2-15 based counter electrode displays a higher electrocatalytic activity towards tri-iodide reduction. Moreover, the Nyquist plots of MoS_2-15 based DSSC under illumination were also recorded, as shown in Fig. S3.† Compared with the results under dark conditions, the impedance at the interface of the counter electrode/electrolyte becomes slightly smaller under illumination, while the charge transfer at the interface of the TiO_2/dye/electrolyte changes a lot. This can be ascribed to the small recombination resistance owing to the introduction of light, especially at the interface of the TiO_2/dye/electrolyte.

In order to exclude the working electrode effect, a symmetrical electrochemical cell with the structure of MoS_2-15/electrolyte/MoS_2-15 was fabricated and used for EIS analysis. Fig. S4a† shows the Nyquist plot of the symmetrical electrochemical cell. The equivalent circuit diagram for fitting the EIS curve is shown in Fig. S4b.† Like the EIS result of the corresponding DSSC, the high-frequency semicircle in the EIS of the symmetrical electrochemical cell reveals the charge transfer process at the electrode/electrolyte interface. The fitting results of the Nyquist plot in Fig. S4a are shown in Table S1.† The EIS parameters of $2R_s$, $2R_{ct}$, and $1/2C_\mu$ are found to be 52.5 Ω, 10.1 Ω, and 16.1 μF, respectively, which are comparable with the EIS data of the MoS_2-15 based DSSC (Table 1) and further confirm the superior electrocatalytic activity of the MoS_2-15 based counter electrode.

An effective surface area is an important factor for the estimation of catalytic activity. Normally, the effective surface area is expected to be linearly proportional to the electrochemical double layer capacitance. The relative effective surface areas of Pt-based and MoS_2-15 based counter electrodes were measured by the CV method in 0.5 M H_2SO_4 aqueous solution, as shown in Fig. S5a and b.† The electrochemical double layer capacitances can be estimated from the slopes of the curves in Fig. 4e, which represent the halves of the positive and negative current density differences at the center of the potential ranges *vs.* the voltage scan rates. Clearly, the capacitance of the MoS_2-15 based counter electrode is much larger than that of the Pt-based counter electrode within the same potential range. This indicates that the MoS_2-15 based counter electrode has a larger effective surface area than the Pt-based counter electrode, which is beneficial for its catalytic activity towards tri-iodide reduction.

To further investigate the electrocatalytic activity for tri-iodide reduction, CV curves of the platinized-FTO, MoS_2-10

based and MoS_2-15 based FTO counter electrodes were measured using a three-electrode system at a scanning rate of 100 mV s^{-1}, respectively (Fig. 4f). For all three CV curves, two pairs of redox peaks were observed. The left peak pair represents the redox transition between I_3^- and I^-, while the right peak pair represents the I_2–I_3^- transition.[30] The electrocatalytic activity of the counter electrode material in a DSSC is directly related to the oxidation–reduction peaks on the left. Typically, the cathodic and anodic peaks on the left can be assigned to the reduction of I_3^- and the oxidation of I^-, respectively. As shown in Fig. 4f, the MoS_2-10 based and MoS_2-15 based counter electrodes show similar anodic and cathodic peaks compared to the Pt-based counter electrode, which indicates that these three electrodes are almost equally effective for tri-iodide reduction. The peak-to-peak separation (E_{pp}) and peak current densities of the left peak pair are two important parameters for analyzing the catalytic activity of the counter electrodes. The E_{pp} values of the Pt based, MoS_2-10 based, and MoS_2-15 based counter electrodes were measured to be 0.47, 0.55, and 0.51 mV, respectively, suggesting that the catalytic activity of the MoS_2-10 based counter electrode is lower than those of the Pt and MoS_2-15 based counter electrodes. On the other hand, compared with Pt and MoS_2-10 based counter electrodes, the MoS_2-15 based counter electrode displays the highest current density at the anodic and cathodic peaks (Fig. 4f), indicating its excellent electrocatalytic activity. This enhancement can be ascribed to the considerably increased surface area of MoS_2 nanofilms in the MoS_2-15 sample. Accordingly, the MoS_2-15 based counter electrode shows higher catalytic activity than the Pt-based counter electrode. Moreover, the cycle performances of Pt and MoS_2-15 based counter electrodes were measured by CV curves at a scanning rate of 100 mV s^{-1}, as shown in Fig. S6.† Similar to the Pt electrode, the CV curve of the MoS_2-15 based counter electrode after 50 cycles almost completely overlaps with its initial CV curve. This indicates that the MoS_2-15 based counter electrode has a good stability to remain intact after repeated cycling.

More CV curves of the Pt-based, MoS_2-10 based and MoS_2-15 based counter electrodes were measured at various scan rates (20, 40, 60, 80, and 100 mV s^{-1}), respectively, as shown in Fig. 5a–c. For all three counter electrodes, it can be clearly observed that the peak current density increases with the scan rate, which is mainly due to the thinner diffusion layer and the larger electrochemical polarization. Moreover, as the scan rate increases, the anodic and cathodic peaks shift positively and negatively, respectively. Based on the data in Fig. 5a–c, the profiles of the anodic and cathodic peak current densities of the left peak pairs *versus* the square root of the scan rates were plotted, as shown in Fig. 5d. The peak current densities of all three counter electrodes display a linear relationship with the square root of the scan rates, indicating that the redox reactions happening on the two MoS_2-based counter electrodes are dominated by diffusion-controlled ion transport as in the case of the Pt-based counter electrode. Furthermore, the linear relationship suggests that there is no specific interaction

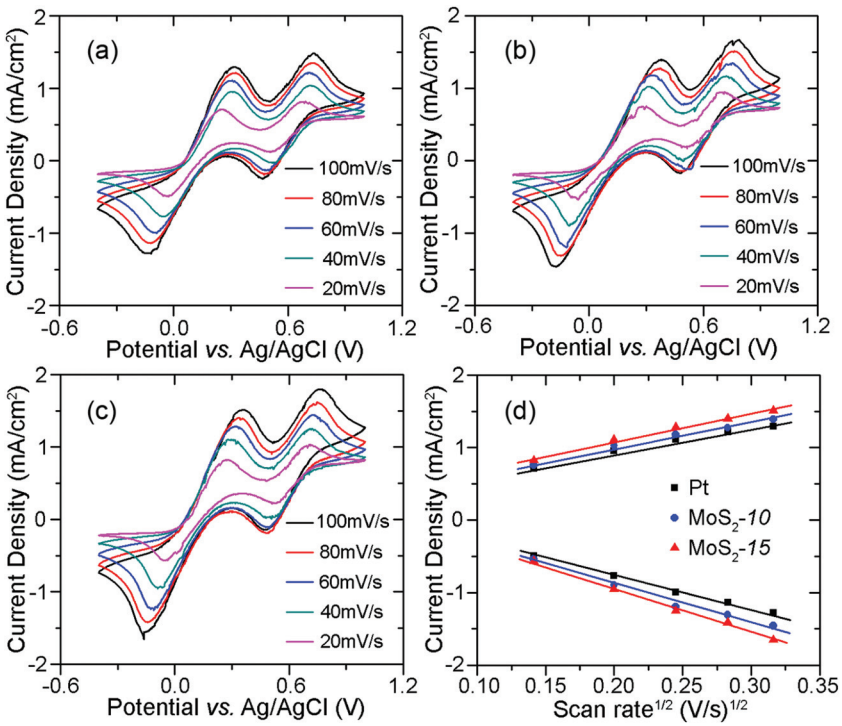

Fig. 5 CV curves of (a) Pt-based, (b) MoS_2-10 based, and (c) MoS_2-15 based counter electrodes at various scanning rates (20, 40, 60, 80, and 100 mV s^{-1}), respectively. (d) The relationship between the peak current density of the left peak pair and the square root of the scan rates.

between the redox couple and the MoS_2-based counter electrodes as in the case of the Pt-based counter electrode.

In summary, the direct growth of large-area and ultrathin MoS_2 nanofilms on FTO glass substrates was achieved by a facile and low-cost solution-phase process. The MoS_2-based counter electrodes exhibited an excellent catalytic activity for tri-iodide reduction according to the EIS and CV curves. When the MoS_2-based counter electrode was used in the DSSC, it displayed an impressive photovoltaic performance as high as 8.3%, which was better than that of the DSSC based on the Pt-based counter electrode. The successful fabrication of the MoS_2-based counter electrode with this greatly simplified preparation process to replace platinum can greatly decrease the manufacturing cost, promote the practical application of DSSCs and also provide a new insight for synthesizing novel counter electrodes with superior photovoltaic performances based on 2D nanomaterials.

Experimental methods

Direct fabrication of ultrathin MoS_2 nanofilms on a transparent conductive glass

Ultrathin MoS_2 nanofilms were grown directly on fluorine-doped tin oxide (FTO) glass substrates by a facile and low-cost solution-phase approach. Typically, a FTO glass was sequentially cleaned by ultrasonication in acetone, ethanol and deionized (DI) water for 5 min. The FTO substrate was put into a Teflon-lined stainless steel autoclave, which contains 30 mg sodium molybdate (Na_2MoO_4) and 60 mg thioacetamide (C_2H_5NS) dissolved in 30 mL DI water. The autoclave was placed in an oven and heated under 200 °C for a reaction time of 5–15 h. After the reaction, the autoclave was fetched out from the oven and rapidly cooled under tap water flushing for 10 min. Finally, the FTO substrate was taken out from the autoclave, washed with ethanol, and dried in air. We named MoS_2-x the MoS_2 nanofilm covered FTO counter electrode prepared by this process, where x corresponds to the growth time in the aqueous solution (x = 5, 10 or 15 h).

Fabrication of DSSCs

To investigate the role of MoS_2, DSSCs with MoS_2-x nanofilm covered FTO glass substrates as the counter electrodes were respectively assembled. The photoanodes were fabricated by screen-printing of TiO_2 nanoparticle paste (18NR-T, Dyesol) onto FTO glass substrates. Before assembling the DSSCs, the photoanodes were immersed in a 0.05 M titanium tetrachloride ($TiCl_4$) solution at 70 °C for 30 min, rinsed with DI water and ethanol, and then annealed in air at 450 °C for 30 min. When the temperature was cooled down to 80 °C, the photoanodes were immersed in a 0.3 mM solution of *cis*-di-(thiocyanato)-bis(2,2′-bipyridyl-4,4′-dicarboxylate) ruthenium(II) (N719, Dalian HeptaChromaSolarTech, China) for 24 h. The dye-sensitized photoanodes were sandwiched together with the counter electrodes using a hot-melt Surlyn spacer with a thickness of ~25 μm. The electrolyte solution containing 0.05 M I_2, 1.0 M 1-propyl-3-methylimidazolium iodide, 0.5 M *N*-methylbenzimidazole and 0.1 M guanidinium thiocyanate in acetonitrile was injected into the holes on the reverse side of the counter electrode. As control experiments, traditional DSSCs with pristine FTO and platinized FTO glass counter electrodes were also fabricated under the same conditions.

Fabrication of a symmetrical electrochemical cell

Two MoS_2-15 counter electrodes were separated by a hot-melt Surlyn spacer with a thickness of ~25 μm. A solution of acetonitrile containing 0.05 M I_2, 1.0 M 1-propyl-3-methylimidazolium iodide, 0.5 M *N*-methylbenzimidazole and 0.1 M guanidinium thiocyanate was used as the electrolyte.

Characterization

The morphological features of the samples were examined by scanning electron microscopy (SEM, HITACH S-4800) and transmission electron microscopy (TEM, JEM-2100). Raman spectroscopy was performed with a 488 nm laser excitation using a Renishaw InVia Raman microscope system. To investigate the components of the samples, X-ray photoelectron spectroscopy (XPS) was performed using a PHI-5000 VersaProbe X-ray photoelectron spectrometer with Al Kα X-ray radiation.

The effective surface areas of Pt-based and MoS_2-15 based electrodes were measured using the CV method. Typically, the electrochemical measurements were performed at room temperature using a standard three-electrode setup in 0.5 M H_2SO_4 solution. A Pt-based or MoS_2-15 based electrode was used as the working electrode. A Pt foil and an Ag/AgCl electrode were used as the counter electrode and reference electrode, respectively. The CV curves were measured at different scan rates (20, 40, 60, 80, and 100 mV s^{-1}) on a Chenhua CHI-760 electrochemical workstation.

The catalytic activities of MoS_2-x nanofilms towards tri-iodide reduction were also characterized at room temperature by using a standard three-electrode electrochemical cell setup in an acetonitrile solution containing 0.1 M $LiClO_4$, 10 mM LiI, and 1 mM I_2. The working, counter, and reference electrodes were MoS_2-x nanofilm covered FTO glass substrates, Pt foil, and Ag/AgCl, respectively. The curves of cyclic voltammetry (CV) were also measured at different scan rates (20, 40, 60, 80, and 100 mV s^{-1}) on a Chenhua CHI-760 electrochemical workstation.

The photovoltaic performances of the DSSCs were measured under simulated AM 1.5 G illumination provided by a solar light simulator (Oriel Solar Simulator, Model 91160). The current–voltage characteristics were recorded by using a Keithley 2400 source meter. The EIS data of DSSCs were also measured under dark and full-light conditions, respectively. With the help of Z-view software, the impedance parameters were determined. The active area of the DSSCs in this study is 0.16 cm^2.

Acknowledgements

This work was supported by the National Thousand Young Talents Program of China, the Young Scientists Project of National Basic Research Program of China (973 Program No. 2015CB659300), the National Natural Science Foundation of China (NSFC Grant No. 21403105 and 21573108), the China Postdoctoral Science Foundation (Grant No. 2015M580413 and 2015M580408), the Natural Science Foundation for Young Scholars of Jiangsu Province (Grant No. BK20160647, BK20150571 and BK20150583), the Fundamental Research Funds for the Central Universities and a project funded by the Priority Academic Program Development of Jiangsu Higher Education Institutions (PAPD).

References

1 K. S. Novoselov, A. K. Geim, S. V. Morozov, D. Jiang, Y. Zhang, S. V. Dubonos, I. V. Grigorieva and A. A. Firsov, *Science*, 2004, **306**, 666–669.
2 G. Algara-Siller, O. Lehtinen, F. C. Wang, R. R. Nair, U. Kaiser, H. A. Wu, A. K. Geim and I. V. Grigorieva, *Nature*, 2015, **519**, 443–445.
3 M. Y. Han, B. Oezyilmaz, Y. Zhang and P. Kim, *Phys. Rev. Lett.*, 2007, **98**, 206805.
4 X. Wang, Y. Ouyang, X. Li, H. Wang, J. Guo and H. Dai, *Phys. Rev. Lett.*, 2008, **100**, 206803.
5 J. Liu, T. H. Hsieh, P. Wei, W. Duan, J. Moodera and L. Fu, *Nat. Mater.*, 2014, **13**, 178–183.
6 S. Najmaei, Z. Liu, W. Zhou, X. Zou, G. Shi, S. Lei, B. I. Yakobson, J. C. Idrobo, P. M. Ajayan and J. Lou, *Nat. Mater.*, 2013, **12**, 754–759.
7 Y. Gong, J. Lin, X. Wang, G. Shi, S. Lei, Z. Lin, X. Zou, G. Ye, R. Vajtai, B. I. Yakobson, H. Terrones, M. Terrones, B. K. Tay, J. Lou, S. T. Pantelides, Z. Liu, W. Zhou and P. M. Ajayan, *Nat. Mater.*, 2014, **13**, 1135–1142.
8 V. K. Sangwan, D. Jariwala, I. S. Kim, K. S. Chen, T. J. Marks, L. J. Lauhon and M. C. Hersam, *Nat. Nanotechnol.*, 2015, **10**, 403–406.
9 Q. Ding, F. Meng, C. R. English, M. Caban-Acevedo, M. J. Shearer, D. Liang, A. S. Daniel, R. J. Hamers and S. Jin, *J. Am. Chem. Soc.*, 2014, **136**, 8504–8507.
10 D. Yoo, M. Kim, S. Jeong, J. Han and J. Cheon, *J. Am. Chem. Soc.*, 2014, **136**, 14670–14673.
11 X. Yin, Z. Ye, D. A. Chenet, Y. Ye, K. O'Brien, J. C. Hone and X. Zhang, *Science*, 2014, **344**, 488–490.
12 D. Y. Qiu, F. H. da Jornada and S. G. Louie, *Phys. Rev. Lett.*, 2013, **111**, 216805.
13 A. K. Singh, S. Andleeb, J. Singh, H. T. Dung, Y. Seo and J. Eom, *Adv. Funct. Mater.*, 2014, **24**, 7125–7132.
14 W. Zhang, J. K. Huang, C. H. Chen, Y. H. Chang, Y. J. Cheng and L. J. Li, *Adv. Mater.*, 2013, **25**, 3456–3461.
15 X. Zou, J. Wang, C. H. Chiu, Y. Wu, X. Xiao, C. Jiang, W. W. Wu, L. Mai, T. Chen, J. Li, J. C. Ho and L. Liao, *Adv. Mater.*, 2014, **26**, 6255–6261.
16 H. Wang, L. Yu, Y. H. Lee, Y. Shi, A. Hsu, M. L. Chin, L. J. Li, M. Dubey, J. Kong and T. Palacios, *Nano Lett.*, 2012, **12**, 4674–4680.
17 D. Kufer, I. Nikitskiy, T. Lasanta, G. Navickaite, F. H. L. Koppens and G. Konstantatos, *Adv. Mater.*, 2015, **27**, 176–180.
18 S. H. Choi, Y. N. Ko, J. K. Lee and Y. C. Kang, *Adv. Funct. Mater.*, 2015, **25**, 1780–1788.
19 X. Xie, Z. Ao, D. Su, J. Zhang and G. Wang, *Adv. Funct. Mater.*, 2015, **25**, 1393–1403.
20 T. Stephenson, Z. Li, B. Olsen and D. Mitlin, *Energy Environ. Sci.*, 2014, **7**, 209–231.
21 J. M. Jeong, K. G. Lee, S. J. Chang, J. W. Kim, Y. K. Han, S. J. Lee and B. G. Choi, *Nanoscale*, 2015, **7**, 324–329.
22 Y. Jiang, X. Li, S. Yu, L. Jia, X. Zhao and C. Wang, *Adv. Funct. Mater.*, 2015, **25**, 2693–2700.
23 S. Xu, D. Li and P. Wu, *Adv. Funct. Mater.*, 2015, **25**, 1127–1136.
24 Y. Yan, X. Ge, Z. Liu, J. Y. Wang, J. M. Lee and X. Wang, *Nanoscale*, 2013, **5**, 7768–7771.
25 X. Zhao, H. Zhua and X. Yang, *Nanoscale*, 2014, **6**, 10680–10685.
26 X. Geng, W. Wu, N. Li, W. Sun, J. Armstrong, A. Al-hilo, M. Brozak, J. Cui and T. Chen, *Adv. Funct. Mater.*, 2014, **24**, 6123–6129.
27 L. Liao, J. Zhu, X. Bian, L. Zhu, M. D. Scanlon, H. H. Girault and B. Liu, *Adv. Funct. Mater.*, 2013, **23**, 5326–5333.
28 B. Hinnemann, P. G. Moses, J. Bonde, K. P. Jorgensen, J. H. Nielsen, S. Horch, I. Chorkendorff and J. K. Norskov, *J. Am. Chem. Soc.*, 2005, **127**, 5308–5309.
29 T. F. Jaramillo, K. P. Jorgensen, J. Bonde, J. H. Nielsen, S. Horch and I. Chorkendorff, *Science*, 2007, **317**, 100–102.
30 J. Zhang, S. Najmaei, H. Lin and J. Lou, *Nanoscale*, 2014, **6**, 5279–5283.
31 S. Jiang, X. Yin, J. Zhang, X. Zhu, J. Li and M. He, *Nanoscale*, 2015, **7**, 10459–10464.
32 B. Lei, G. R. Li and X. P. Gao, *J. Mater. Chem. A*, 2014, **2**, 3919–3925.
33 J. Y. Lin, C. Y. Chan and S. W. Chou, *Chem. Commun.*, 2013, **49**, 1440–1442.
34 C. J. Liu, S. Y. Tai, S. W. Chou, Y. C. Yu, K. D. Chang, S. Wang, F. S. S. Chien, J. Y. Lin and T. W. Lin, *J. Mater. Chem.*, 2012, **22**, 21057–21064.
35 S. Y. Tai, C. J. Liu, S. W. Chou, F. S. S. Chien, J. Y. Lin and T. W. Lin, *J. Mater. Chem.*, 2012, **22**, 24753–24759.
36 G. Yue, J. Wu, Y. Xiao, M. Huang, J. Lin and J. Y. Lin, *J. Mater. Chem. A*, 2013, **1**, 1495–1501.
37 M. Wu, Y. Wang, X. Lin, N. Yu, L. Wang, L. Wang, A. Hagfeldt and T. Ma, *Phys. Chem. Chem. Phys.*, 2011, **13**, 19298–19301.
38 J. Plummer, *Nat. Mater.*, 2015, **14**, 1186.
39 Y. B. Chen, J. Y. Sun, J. F. Gao, F. Du, Q. Han, Y. F. Nie, Z. L. Chen, A. Bachmatiuk, M. K. Priydarshi, D. L. Ma,

X. J. Song, X. S. Wu, C. Y. Xiong, M. H. Rummeli, F. Ding, Y. F. Zhang and Z. F. Liu, *Adv. Mater.*, 2015, **27**, 7839–7846.

40 H. T. Wang, Z. Y. Lu, S. C. Xu, D. S. Kong, J. J. Cha, G. Y. Zheng, P. C. Hsu, K. Yan, D. Bradshaw, F. B. Prinz and Y. Cui, *Proc. Natl. Acad. Sci. U. S. A.*, 2013, **110**, 19701–19706.

41 T. W. Hamann, R. A. Jensen, A. B. F. Martinson, H. Van Ryswyk and J. T. Hupp, *Energy Environ. Sci.*, 2008, **1**, 66–78.

42 Y. Lin, X. Ling, L. Yu, S. Huang, A. L. Hsu, Y. H. Lee, J. Kong, M. S. Dresselhaus and T. Palacios, *Nano Lett.*, 2014, **14**, 5569–5576.

43 Q. Xiang, J. Yu and M. Jaroniec, *J. Am. Chem. Soc.*, 2012, **134**, 6575–6578.